Nanoscale

PAPER

View Article Online
View Journal | View Issue

Cite this: *Nanoscale*, 2024, **16**, 1733

Modification of an oxyhalide solid-solution photocatalyst with an efficient O_2-evolving cocatalyst and electron mediator for two-step photoexcitation overall water splitting†

Wenzheng Sun, [a,b] Ying Luo,[a,b] Jun Xu,[a,b] Qiaoqi Guo,[a,b] Lidan Deng,[c] Zheng Wang *[a,b] and Hong He *[a,b]

Two-step photoexcitation overall water splitting based on particulate photocatalysts represents a promising approach for low-cost solar hydrogen production. The performance of an O_2-evolution photocatalyst and electron mediator between two photocatalysts crucially influences the construction of an efficient two-step excitation water-splitting system. Bismuth–tantalum oxyhalides are emerging photocatalysts for O_2 evolution reactions and can be applied in two-step water-splitting systems. In this study, a highly crystalline $Bi_4TaO_8Cl_{0.9}Br_{0.1}$ solid solution with microplatelet morphology was synthesized by the dual flux method. The light absorption intensity and charge transfer efficiency of the $Bi_4TaO_8Cl_{0.9}Br_{0.1}$ solid solution were higher than those of Bi_4TaO_8Cl and Bi_4TaO_8Br; thus, the sacrificial O_2 evolution activity of $Bi_4TaO_8Cl_{0.9}Br_{0.1}$ photocatalyst was obviously enhanced. The two-step excitation water splitting with a solid-state electron mediator was successfully constructed using $Bi_4TaO_8Cl_{0.9}Br_{0.1}$ as the O_2-evolution photocatalyst and Ru/$SrTiO_3$:Rh as the H_2-evolution photocatalyst. The CoO_x cocatalyst and reduced graphene oxide decorations on the surface of $Bi_4TaO_8Cl_{0.9}Br_{0.1}$ promoted the catalytic O_2 generation process on $Bi_4TaO_8Cl_{0.9}Br_{0.1}$ and electron transfer between CoO_x/$Bi_4TaO_8Cl_{0.9}Br_{0.1}$ and Ru/$SrTiO_3$:Rh photocatalysts, respectively. As a result, the apparent quantum yield for this overall water-splitting system was 1.26% at 420 nm, which surpassed the present performance of the two-step excitation water-splitting systems consisting of metal oxyhalide photocatalysts. This study demonstrates the validity of high-quality solid-solution photocatalysts with suitable surface modification for efficient solar hydrogen production from water splitting.

Received 30th October 2023,
Accepted 19th December 2023

DOI: 10.1039/d3nr05498e

rsc.li/nanoscale

Introduction

Solar water splitting using semiconductor particulate photocatalysts for sustainable hydrogen production is one of the promising solutions to tackle the constantly increasing global energy demand and related environmental issues.[1–3] However, the large-scale utilization of inexhaustible solar energy faces a series of challenges, the most important being how to attain significant improvement in the efficiency of solar to hydrogen conversion. Under these circumstances, many efficient particulate photocatalysts with narrow bandgaps for water splitting have been extensively explored and achieved immense development of efficient water splitting.[4–10] These attempts are mainly accomplished through two approaches, namely, one-step photoexcitation overall water splitting on a single photocatalyst and two-step photoexcitation overall water splitting mimicking photosynthesis in a green plant.[11] For one-step photoexcitation water splitting, a lot of metal oxide photocatalysts were active under UV irradiation.[11] In order to utilize the solar spectrum over a wide wavelength range, some visible-light-responsive photocatalysts within the (oxy)nitrides,[8,12] cation-doped oxides[4] and plasmon photocatalysts[13] have been reported to function in one-step excitation water splitting. However, the stringent requirements, such as the sufficient band gap and band position and efficient separation and transport of electron–hole pairs, limit the application of various visible-light-driven photocatalysts.[11] Thus, two-step photoexcitation water splitting composed of an H_2-evolution photocatalyst (HEP) and O_2-evolution photocatalyst (OEP) allows the construction

[a]*State Key Joint Laboratory of Environment Simulation and Pollution Control, Research Center for Eco-Environmental Sciences, Chinese Academy of Sciences, Beijing 100085, China. E-mail: zhengwang@rcees.ac.cn, honghe@rcees.ac.cn*
[b]*University of Chinese Academy of Sciences, Beijing 100049, China*
[c]*School of Energy and Power Engineering, Huazhong University of Science and Technology, Wuhan 430074, China*

† Electronic supplementary information (ESI) available. See DOI: https://doi.org/10.1039/d3nr05498e

of efficient photocatalytic water splitting systems using an increasing number of visible-light-driven photocatalysts.[14–16] The O_2-evolution reaction involving a four-electron transfer process is generally regarded as a rate-determining step in the water splitting reaction; therefore, it is crucial to develop efficient OEPs to improve the performance of two-step excitation water splitting.[17–20]

Among various visible-light-driven OEPs, Sillén–Aurivillius perovskite-phase oxyhalides, a series of emerging photocatalyst materials, have been studied for Z-scheme water splitting[21–24] as well as for H_2 or O_2 evolution half-reactions using sacrificial reagents.[25–28] As a kind of bismuth-based oxyhalides, Bi_4TaO_8Cl[22,29] and Bi_4TaO_8Br[21,30] with the simple layered structures and narrow band gap exhibit outstanding properties in the O_2-evolution reaction because of longer charge transfer distance, stability against photocorrosion and potential of extensive band engineering.[21,26,31] The hybridization of O 2p orbitals with Bi 6s orbitals in Bi_4TaO_8Cl and Bi_4TaO_8Br results in the upward shift of the valence band maximum, which effectively brings the visible light absorption and the photoexcited charge migration promotion.[21,25] Moreover, the predominant contribution of O 2p orbitals for valence band maximum allows Bi_4TaO_8Cl and Bi_4TaO_8Br to stably produce O_2 from water oxidation.[21] It is worth noting that Cl 3p orbitals in Bi_4TaO_8Cl and Br 4p orbitals in Bi_4TaO_8Br exhibit different energy levels located in the valence band.[25] Therefore, the construction of a bismuth-based oxyhalide solid solution using Cl and Br anions will be beneficial for the charge carrier migration towards efficient O_2-evolution reaction.

In a two-step photoexcitation water-splitting system, electron transfer from OEPs to HEPs is also an important issue in determining the system's performance.[32] Traditionally, ionic redox shuttle couples such as Fe^{3+}/Fe^{2+}, IO_3^-/I^- and $[Fe(CN)_6]^{3-}/[Fe(CN)_6]^{4-}$ functioning as electron mediators, are necessary building blocks to construct a two-step photoexcitation water splitting system.[5,19,21,31,33,34] In the recent work, a Fe^{3+}/Fe^{2+} redox couple was reported as an active electron mediator in the two-step excitation water splitting with Bi_4NbO_8Cl or Bi_4TaO_8X (X = Cl, Br) as OEP.[21,31] However, the existence of ionic redox couples in the reaction solution unavoidably leads to backward reactions consuming the photogenerated electrons and holes from HEPs and OEPs, respectively, and a shielding effect for incident light.[35] On account of the disadvantages, the solid-state conductive mediators instead of ionic redox couples are applied in the two-step photoexcitation water splitting systems to achieve highly efficient charge transfer between OEPs and HEPs. Au,[36] carbon,[37] indium tin oxide,[38] Ir,[39] and reduced graphene oxide (RGO)[32,40,41] working as efficient electron mediators have been demonstrated to boost outstanding overall water splitting activity in the two-step excitation photocatalyst sheet systems or suspension systems. Therefore, it is desirable to promote charge transfer efficiency in the two-step photoexcitation water splitting system with bismuth-based oxyhalide OEP by combining the RGO solid-state mediator.

Herein, we present a well-crystallized $Bi_4TaO_8Cl_{0.9}Br_{0.1}$ solid solution for photocatalytic O_2 evolution and construct a two-step photoexcitation water splitting system by combining it with $Ru/SrTiO_3$:Rh as an HEP and RGO as the solid electron mediator. The incorporation of Br^- into the layered Bi_4TaO_8Cl enhanced the light absorption intensity and facilitated charge separation and migration, thus, the O_2-evolution rate of $Bi_4TaO_8Cl_{0.9}Br_{0.1}$ using Fe^{3+} as the electron sacrificial reagent reached 102 μmol h^{-1} under visible light irradiation. Furthermore, $Bi_4TaO_8Cl_{0.9}Br_{0.1}$ solid solution exhibited higher activity for two-step photoexcitation water splitting than Bi_4TaO_8Cl or Bi_4TaO_8Br as OEP. Upon the modification of $Bi_4TaO_8Cl_{0.9}Br_{0.1}$ with the O_2-evolution cocatalyst and solid-state electron mediator, CoO_x as O_2-evolution cocatalyst and RGO as solid-state conductor dramatically improved the O_2 formation process on $Bi_4TaO_8Cl_{0.9}Br_{0.1}$ and electron transfer between photocatalysts, resulting in an apparent quantum yield (AQY) of 1.26% at 420 nm for the two-step photoexcitation water splitting system.

Zheng Wang

Zheng Wang received his PhD under the supervision of Prof. Tsunehiro Tanaka in the Department of Molecular Engineering at Kyoto University in 2015. Then he moved to Prof. Kazunari Domen's group at the University of Tokyo and Shinshu University as the ARPChem project researcher. Since 2020, he joined in Research Center for Eco-Environmental Sciences at Chinese Academy of Sciences as a professor and group leader. He is interested in the utilization and conversion of carbon dioxide and water splitting based on the photocatalysis, photoelectrochemical and photothermocatalysis process.

Experimental section

Preparation of materials

$Bi_4TaO_8Cl_{0.9}Br_{0.1}$ and $Bi_4TaO_8Cl_{0.5}Br_{0.5}$ powders were prepared by a flux method. Stoichiometric quantities of Bi_2O_3, BiOCl, BiOBr, and Ta_2O_5 were mixed, and NaCl and KCl (molar ratio of NaCl/KCl is 1 : 1) were used as flux reagents. The fluxes were mixed with Bi_2O_3, BiOCl, BiOBr, and Ta_2O_5 at a solute concentration of 10 mol%. The mixture was ground in an agate mortar for 30 min and placed in an alumina crucible and calcined in a muffle furnace at 923 K for 14 h at a heating rate of 10 K min^{-1}. $Bi_4TaO_8Cl_{0.9}Br_{0.1}$ and $Bi_4TaO_8Cl_{0.5}Br_{0.5}$ obtained in this manner were washed with deionized water several times and collected by filtration to remove residual flux reagents. The yellow powder was then dried at room tempera-

ture. For comparison, Bi_4TaO_8Cl and Bi_4TaO_8Br samples were prepared using the same procedure.

Rh-doped $SrTiO_3$ ($SrTiO_3$:Rh) HEP was prepared by the solid state reaction method.[42] $SrCO_3$, TiO_2, and Rh_2O_3 were mixed in a mortar at the ratio of Sr : Ti : Rh = 1.03 : 0.99 : 0.01 and ground for 30 min. The mixture was calcined in a muffle furnace at 1273 K for 10 h in the air using an alumina crucible to obtain $SrTiO_3$:Rh (1%) powder.

Modification of photocatalysts

Firstly, CoO_x, IrO_x, RuO_x, and PtO_x were loaded on the obtained metal oxyhalides as cocatalysts for water oxidation by impregnation using aqueous solutions containing $Co(NO_3)_2$, Na_2IrCl_6, $RuCl_3$ or H_2PtCl_6. Specifically, metal oxyhalide powder (0.22 g) was immersed in an aqueous solution containing the required amount of cocatalyst-precursor solution. The slurry was stirred with sonication for 3 min and then dried by a hot water bath, the resulting mixture was heated at 573–873 K for 2 h in air. Subsequently, metal oxyhalides modified with MO_x (M = Co, Ir, Ru, and Pt) cocatalysts were further decorated with graphene oxide by the photodeposition method. Photocatalyst powders and graphene oxide dispersion were suspended in 20 vol% of the aqueous methanol solution. The reaction solution was evacuated to completely remove air and irradiated under visible light ($\lambda \geq 420$ nm) for 2 h to form RGO on photocatalyst powders. Metal oxyhalides loaded with MO_x (M = Co, Ir, Ru, and Pt) cocatalyst were also modified with metallic Ir or Au conductive mediator by the impregnation method followed by the H_2-reduction treatment. The loading amount of Ir or Au was 0.3 wt%. Pt-modified metal oxyhalide photocatalysts were synthesized by impregnation with H_2-reduction treatment, and the Pt content was 0.3 wt%.

As for the modification of $SrTiO_3$:Rh, Ru (0.7 wt%) cocatalyst was loaded by the photodeposition method in an aqueous methanol solution (20 vol%) containing the required amount of the Ru precursor under visible light irradiation ($\lambda \geq 420$ nm) for 6 h, denoted as Ru/$SrTiO_3$:Rh.

Characterization of materials

X-ray diffraction (XRD) patterns were obtained using a Bruker D8 Advance X-ray diffractometer with Cu Kα radiation source, operating at 40 kV and 40 mA. Scanning electron microscopy (SEM) images and elemental mapping images were acquired using a Hitachi SU-8020 field-emission scanning electron microscope equipped with an energy dispersive spectrometer (Bruker Nano GmbH). UV-vis diffuse reflectance spectra (DRS) were collected using a spectrophotometer (LAMBDA 650S, PerkinElmer) equipped with an integrating sphere. The binding energies were determined by X-ray photoelectron spectroscopy (XPS) on a Thermo Scientific ESCALAB 250Xi spectrometer with a monochromatic Al Kα source ($h\nu$ = 1486.6 eV) and normalized to C 1s for each sample.

Photoelectrochemical measurements

Photoelectrochemical measurements were performed at room temperature using a CHI 650E electrochemical workstation with a standard three-electrode cell. The prepared electrode, an Ag/AgCl electrode, and Pt wire were used as the working electrode, reference electrode, and counter electrode, respectively. The working electrodes of bare metal oxyhalides and surface-modified metal oxyhalides were prepared by a conventional drop-casting method. The photocurrents of bare metal oxyhalides and surface-modified metal oxyhalides electrodes were measured in an 0.1 M Na_2SO_4 solution (pH = 7) bubbling with Ar gas under visible light irradiation ($\lambda \geq 420$ nm, 300 W Xe lamp) at 0.8 V *vs.* RHE. Electrochemical impedance spectroscopy (EIS) was recorded in the frequency range of 10^5 Hz to 0.1 Hz with the initial potential (0.01 V) in 0.1 M Na_2SO_4 solution.

Photocatalytic activity measurements

The photocatalytic O_2 evolution reaction was performed in a gas-closed circulation system with a Pyrex top-illuminated reaction vessel. Pt-modified metal oxyhalide photocatalysts (100 mg) were dispersed in 150 ml of 10 mM aqueous Fe $(NO_3)_3$ solution. The reaction temperature was maintained at 285 K by circulating cold water. After completely removing air from the reaction system by evacuation, 10 kPa Ar gas was introduced into the reaction system, and the slurry was irradiated under a 300 W Xenon lamp equipped with a cutoff filter ($\lambda \geq 420$ nm). The gas products were measured by an online thermal conductivity detector-gas chromatography system equipped with a Molecular Sieve 5 Å column using Ar as the carrier gas. Two-step excitation water splitting was carried out under similar experimental conditions except that Ru-modified $SrTiO_3$:Rh (50 mg) as HEP and surface-modified metal oxyhalide as OEP were dispersed in deionized water (150 ml) by adjusting the pH with H_2SO_4.

Apparent quantum yield measurements

The apparent quantum yield (AQY) of two-step photoexcitation water splitting was measured using a 300 W Xenon lamp equipped with a 420 nm band-pass filter. The AQY was calculated using the following equation:

$$\mathrm{AQY}(\%) = [4 \times n(\mathrm{H_2})]/n(\mathrm{photons}) \times 100$$

where $n(H_2)$ and n(photons) represent the number of H_2 molecules generated in the two-step photoexcitation water splitting and the number of incident photons, respectively.

Results and discussion

The XRD patterns in Fig. 1a show that Bi_4TaO_8Cl and Bi_4TaO_8Br synthesized by the flux method were pure phases of the Sillén–Aurivillius layered perovskite structure and the different diffraction peak positions of Bi_4TaO_8Cl and Bi_4TaO_8Br were due to the anionic sizes of Cl^- and Br^- in the crystal structure. For $Bi_4TaO_8Cl_{0.9}Br_{0.1}$ and $Bi_4TaO_8Cl_{0.5}Br_{0.5}$, pure phases of the layered perovskite structure were observed and the diffraction peaks were located between those of Bi_4TaO_8Cl and Bi_4TaO_8Br, which indicated the formation of

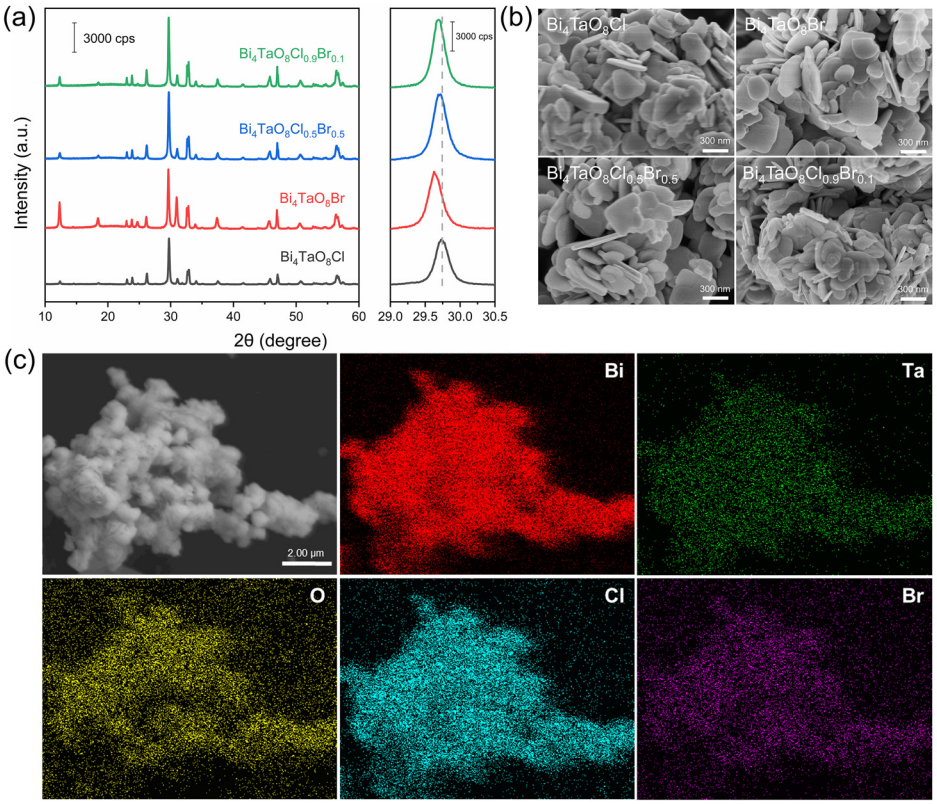

Fig. 1 (a) XRD patterns and (b) SEM images of Bi_4TaO_8Cl, Bi_4TaO_8Br, $Bi_4TaO_8Cl_{0.5}Br_{0.5}$, and $Bi_4TaO_8Cl_{0.9}Br_{0.1}$. (c) EDS elemental mapping of $Bi_4TaO_8Cl_{0.9}Br_{0.1}$.

the solid solution containing Cl and Br anions. Moreover, the higher XRD peak intensities of the solid solution samples in comparison to Bi_4TaO_8Cl and Bi_4TaO_8Br demonstrated that $Bi_4TaO_8Cl_{0.9}Br_{0.1}$ and $Bi_4TaO_8Cl_{0.5}Br_{0.5}$ were well-crystallized, because the dual fluxes promoted the sufficient diffusion of precursor ions, allowing the rapid growth of single phase at low temperature.[43] The morphology of the as-prepared samples is shown in SEM images of Fig. 1b and Fig. S1.† Four samples displayed similar microplatelet morphology with 200–500 nm in size and 50–100 nm in thickness. $Bi_4TaO_8Cl_{0.9}Br_{0.1}$ sample exhibited relatively small and thin plates. However, due to the calcination and intrinsic characteristics of the layered crystal structure, the aggregations of particulates were observed for all samples.[21] The uniform dispersions of Bi, Ta, O, Cl, and Br atoms shown in Fig. 1c also indicate that $Bi_4TaO_8Cl_{0.9}Br_{0.1}$ were homogeneous solid solutions.

The UV-vis DRS of the oxyhalide samples shown in Fig. 2a indicates that the absorption edge of Bi_4TaO_8Cl, and $Bi_4TaO_8Cl_{0.9}Br_{0.1}$ was approximately at 474 nm and the absorption edge of Bi_4TaO_8Br and $Bi_4TaO_8Cl_{0.5}Br_{0.5}$ was approximately at 469 nm. Although the absorption edge and band structures of the four samples are not very different from each other due to the small contribution of the halogen orbitals to the valence band maximum of Bi_4TaO_8X (X = Cl, Br),[21] the light absorption intensity for Bi_4TaO_8Cl and $Bi_4TaO_8Cl_{0.9}Br_{0.1}$ oxyhalides mainly containing Cl^- anions was obviously higher than that for Bi_4TaO_8Br and $Bi_4TaO_8Cl_{0.5}Br_{0.5}$, including higher Br^- contents. The photocurrent and EIS measurements were carried out and the results are shown in Fig. 2b and c. In comparison to Bi_4TaO_8Cl, Bi_4TaO_8Br, and $Bi_4TaO_8Cl_{0.5}Br_{0.5}$, $Bi_4TaO_8Cl_{0.9}Br_{0.1}$ exhibited a higher photocurrent density for photoelectrochemical water oxidation reactions and lower electrochemical resistance, indicating the formation of $Bi_4TaO_8Cl_{0.9}Br_{0.1}$ solid solution with the small Br^- content promoting the photogenerated charge separation and diffusion in the bulk. The O_2-evolution performance of the Pt-modified oxyhalide photocatalysts was evaluated in the aqueous $Fe(NO_3)_3$ solution under the irradiation of visible light, as shown in Fig. 2d and Fig. S2.† The $Bi_4TaO_8Cl_{0.9}Br_{0.1}$ sample exhibited a superior O_2-evolution activity as compared with the other three oxyhalides, due to high crystallinity, intense light absorption, and rapid charge separation and migration of $Bi_4TaO_8Cl_{0.9}Br_{0.1}$. In addition, the O_2-evolution performance of these oxyhalides was further investigated in a two-step photoexcitation water-splitting reaction. As shown in Fig. 2e and Fig. S3,† when combined with $Ru/SrTiO_3$:Rh as the HEP, $Bi_4TaO_8Cl_{0.9}Br_{0.1}$ showed higher photocatalytic activity for two-step excitation water splitting than the other three oxyhalide photocatalysts. The O_2-evolution activities of four oxyhalide photocatalysts are well correlated in the two-step photoexcitation water splitting and half-reactions using the aqueous $Fe(NO_3)_3$ solution. Moreover, the XRD patterns (Fig. S4†) and

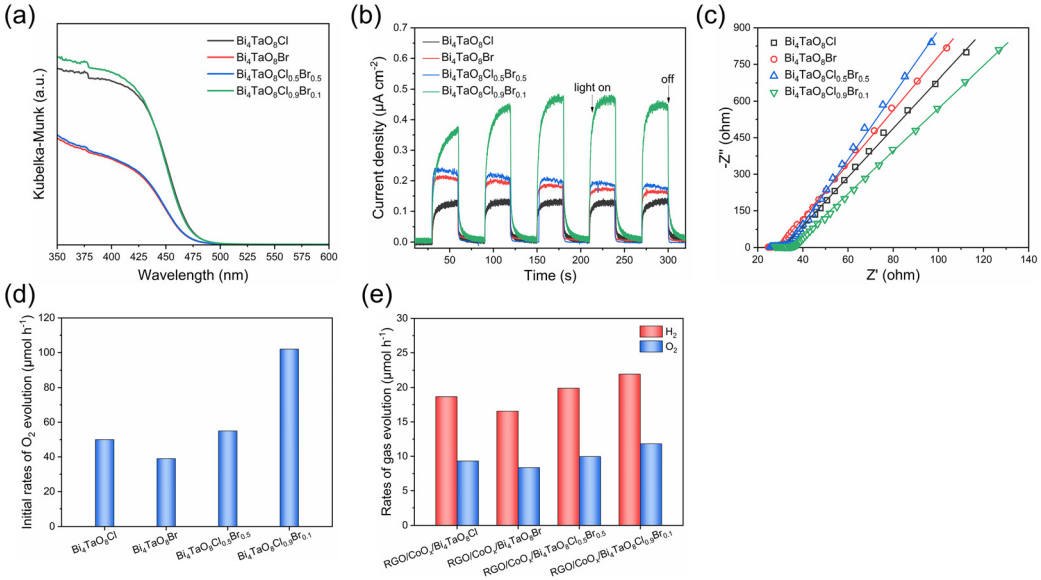

Fig. 2 (a) UV-vis DRS of Bi_4TaO_8Cl, Bi_4TaO_8Br, $Bi_4TaO_8Cl_{0.5}Br_{0.5}$, and $Bi_4TaO_8Cl_{0.9}Br_{0.1}$. (b) Photocurrent for Bi_4TaO_8Cl, Bi_4TaO_8Br, $Bi_4TaO_8Cl_{0.5}Br_{0.5}$, and $Bi_4TaO_8Cl_{0.9}Br_{0.1}$ under visible light ($\lambda \geq 420$ nm) at 0.8 V *vs.* RHE. (c) EIS spectra of Bi_4TaO_8Cl, Bi_4TaO_8Br, $Bi_4TaO_8Cl_{0.5}Br_{0.5}$, and $Bi_4TaO_8Cl_{0.9}Br_{0.1}$. (d) The photocatalytic performance of O_2 evolution on Pt-modified oxyhalide photocatalysts from an aqueous $Fe(NO_3)_3$ solution. Conditions: photocatalyst, 100 mg; cocatalyst, 0.3 wt% Pt; 10 mM aqueous $Fe(NO_3)_3$ solution, 150 mL; light source, 300 W Xenon lamp ($\lambda \geq 420$ nm). (e) H_2 and O_2 evolution rates of two-step excitation overall water splitting reaction using Ru/$SrTiO_3$:Rh as the HEP and surface-modified oxyhalide photocatalysts as the OEP. Conditions: HEP, 50 mg; OEP (CoO_x, 0.5 wt% as Co; RGO, 0.5 wt%), 50 mg; 150 mL H_2O, pH = 4; light source, 300 W Xenon lamp ($\lambda \geq 420$ nm).

EDS elemental mapping (Fig. S5†) of the photocatalysts after the reaction were collected to analyze the Cl and Br species. The same diffraction peak positions for samples before and after the photocatalytic reaction and the uniform distribution of Bi, Ta, O, Cl, and Br elements after the O_2-evolution reaction indicated the stable structure of the $Bi_4TaO_8Cl_{0.9}Br_{0.1}$ solid solution containing Cl and Br anions.

Considering the essential role of the O_2-evolving cocatalyst in the overall water-splitting reaction, the performance of different cocatalysts was examined as shown in Fig. 3 and Fig. S6.† When O_2-evolving cocatalysts were loaded on $Bi_4TaO_8Cl_{0.9}Br_{0.1}$ by calcining at 573 K in air, CoO_x and RuO_x cocatalysts gave higher activity for two-step excitation overall water splitting than IrO_x and PtO_x. Notably, when the calcination temperature of the cocatalyst loading increased to 773 K, the gas evolution rates in the water splitting system using CoO_x-modified $Bi_4TaO_8Cl_{0.9}Br_{0.1}$ became nearly double that of CoO_x-modified $Bi_4TaO_8Cl_{0.9}Br_{0.1}$ calcined at 573 K, whereas the performance improvement of the RuO_x-modified $Bi_4TaO_8Cl_{0.9}Br_{0.1}$ was not so obvious. The results demonstrate that the deposition of the adequate CoO_x cocatalyst on $Bi_4TaO_8Cl_{0.9}Br_{0.1}$ is significant in preventing adverse electron–hole recombination in $Bi_4TaO_8Cl_{0.9}Br_{0.1}$ and boosts the interfacial charge transfer towards the surface O_2-evolution reaction, especially in an all-solid-state system.[44] Accordingly, the effect of the preparation conditions of CoO_x-modified $Bi_4TaO_8Cl_{0.9}Br_{0.1}$ on the water-splitting activity was investigated. Table 1 summarizes the photocatalytic activities for the

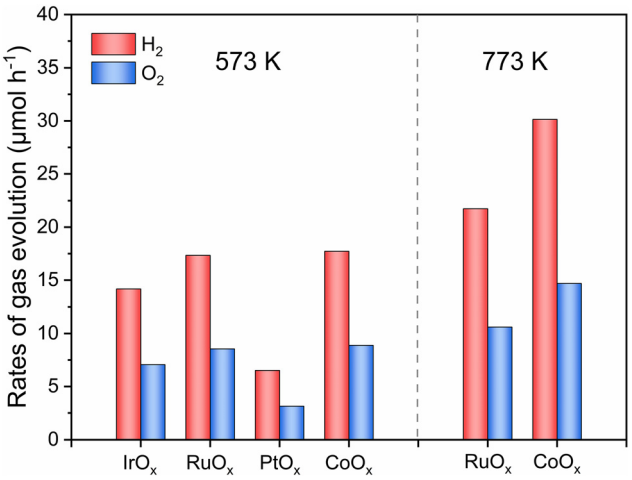

Fig. 3 H_2 and O_2 evolution rates of the two-step excitation overall water splitting reaction using $Bi_4TaO_8Cl_{0.9}Br_{0.1}$ as the OEP modified with different O_2-evolving cocatalysts calcined at different temperatures. Conditions: Ru/$SrTiO_3$:Rh as HEP, 50 mg; surface-modified $Bi_4TaO_8Cl_{0.9}Br_{0.1}$ (IrO_x, RuO_x, PtO_x or CoO_x, 0.5 wt% as Ir, Ru, Pt or Co; RGO, 0.5 wt%), 50 mg; 150 mL H_2O, pH = 4; light source, 300 W Xenon lamp ($\lambda \geq 420$ nm).

two-step excitation overall water splitting reactions consisting of $Bi_4TaO_8Cl_{0.9}Br_{0.1}$ modified with different amounts of CoO_x at different calcination temperatures and time courses of water splitting reactions are shown in Fig. S7 and S8.† The activity

Table 1 Photocatalytic performance for the two-step excitation overall water splitting reaction using CoO_x-modified $Bi_4TaO_8Cl_{0.9}Br_{0.1}$ as OEP prepared using different Co contents and calcination temperatures[a]

Entry	Impregnation–calcination temperature of CoO_x	Amount of CoO_x (wt%)	Evolution rate of H_2 (μmol h^{-1})	Evolution rate of O_2 (μmol h^{-1})
1	573 K	0.5	17.7	8.9
2	673 K	0.5	39.8	19.7
3	773 K	0.5	32.3	15.9
4	873 K	0.5	13.5	7.0
5	673 K	0.3	21.8	10.5
6	673 K	0.8	27.0	13.4
7	673 K	1.0	23.2	11.6

[a] Reaction conditions: Ru/$SrTiO_3$:Rh as HEP, 50 mg; surface-modified $Bi_4TaO_8Cl_{0.9}Br_{0.1}$ (RGO, 0.5 wt%), 50 mg; 150 mL H_2O, pH = 4; light source, 300 W Xenon lamp ($\lambda \geq 420$ nm).

Table 2 Photocatalytic performance for the two-step excitation overall water splitting reaction using different types of electron mediators[a]

Entry	Mediator	Loading amount (wt%)	Evolution rate of H_2 (μmol h^{-1})	Evolution rate of O_2 (μmol h^{-1})
1	RGO	0.1	36.1	17.8
2	RGO	0.3	41.4	20.2
3	RGO	0.5	39.8	19.7
4	RGO	0.7	25.9	13.1
5	Ir	0.3	23.3	13.4
6	Au	0.3	21.2	10.9
7	Fe^{3+}/Fe^{2+}	—	18.5	9.0
8	None	—	17.4	8.7
9	GO	—	12.5	6.6

[a] Reaction conditions: Ru/$SrTiO_3$:Rh as HEP, 50 mg; surface-modified $Bi_4TaO_8Cl_{0.9}Br_{0.1}$ (CoO_x, 0.5 wt% as Co), 50 mg; 150 mL H_2O (150 mL of 2 mM $Fe(NO_3)_3$ solution for entry 7), pH = 4 (pH = 2.4 for entry 7); light source, 300 W Xenon lamp ($\lambda \geq 420$ nm).

was improved with increasing calcination temperature from 573 K to 673 K, reaching a maximum of 673 K, and then decreasing at 773 K and 873 K (entries 1–4). Similarly, $Bi_4TaO_8Cl_{0.9}Br_{0.1}$ loaded with different CoO_x contents exhibited varied activity with volcano-like behavior (entry 2, entries 5–7) and the optimal performance was attained at a Co loading of 0.5 wt%.

Besides the importance of the O_2-evolution cocatalyst on $Bi_4TaO_8Cl_{0.9}Br_{0.1}$, the electron mediator between OEP and HEP also plays a crucial role in the two-step excitation overall water-splitting reaction. Table 2 and Fig. S9, S10† show the influence of different types of electron mediators on the photocatalytic activities of the overall water-splitting system with CoO_x-modified $Bi_4TaO_8Cl_{0.9}Br_{0.1}$ OEP. All solid-state electron conductors exhibited higher photocatalytic overall water-splitting activities than the Fe^{3+}/Fe^{2+} ionic shuttle mediator, indicating that the electron transfer between OEP and HEP and the elimination of the reverse reaction benefited from the solid-state conductive mediator.[32] As compared with metallic Ir and Au mediators, RGO loaded on $Bi_4TaO_8Cl_{0.9}Br_{0.1}$ gave the best photocatalytic performance for two-step excitation water splitting. Furthermore, in comparison to the performance of a two-step excitation water splitting system using RGO as a mediator, the systems without RGO or other conductive mediators and with GO to form physical contact with OEP exhibited much lower activity, which can further demonstrate the significant effect of RGO on the promotion of electron transfer.

Fig. 4a and Fig. S11† show the SEM images of the RGO- and CoO_x-co-modified $Bi_4TaO_8Cl_{0.9}Br_{0.1}$ photocatalyst, in which RGO thin films and CoO_x particles were uniformly dispersed on $Bi_4TaO_8Cl_{0.9}Br_{0.1}$. Moreover, according to the C 1s XPS spectra for the graphene oxide (GO) sample and RGO-modified $Bi_4TaO_8Cl_{0.9}Br_{0.1}$ shown in Fig. 4b, RGO on $Bi_4TaO_8Cl_{0.9}Br_{0.1}$ exhibited much weaker C–O and C=O peaks than the GO sample. These results demonstrate that oxygen-functional groups in the GO sample were reduced by photogenerated electrons from $Bi_4TaO_8Cl_{0.9}Br_{0.1}$ during the photodeposition process[45] and RGO adhered to $Bi_4TaO_8Cl_{0.9}Br_{0.1}$ intimately to facilitate electron transfer.[46] The overall water-splitting activity dependence on the loading amount of RGO was investigated. As shown in Fig. 4c and Fig. S12,† the gas evolution rates increased with the increase of RGO content and reached a maximum at 0.3 wt%, which is because of the efficient electron transfer between Ru/$SrTiO_3$:Rh and CoO_x/$Bi_4TaO_8Cl_{0.9}Br_{0.1}$ mediated by RGO conductor. The activity began to decrease when RGO content was beyond 0.3 wt%, this is due to incident light shielding and active site blocking effects due to the excessive RGO coverage on CoO_x/$Bi_4TaO_8Cl_{0.9}Br_{0.1}$.[45] Furthermore, the photocurrent densities of RGO- and CoO_x-co-modified $Bi_4TaO_8Cl_{0.9}Br_{0.1}$ were one or two orders of magnitude higher than those of pristine $Bi_4TaO_8Cl_{0.9}Br_{0.1}$ and CoO_x-modified $Bi_4TaO_8Cl_{0.9}Br_{0.1}$ without RGO, as shown in Fig. 4d, demonstrating the remarkable promotion of charge transfer by the modification of $Bi_4TaO_8Cl_{0.9}Br_{0.1}$ with the RGO mediator. In addition, the photoelectrochemical performance for the water oxidation of RGO- and CoO_x-co-modified $Bi_4TaO_8Cl_{0.9}Br_{0.1}$ with different RGO contents corresponded well to the overall performance of water splitting reactions shown in Fig. 4c.

Two-step photoexcitation overall water splitting was successfully accomplished with CoO_x-modified $Bi_4TaO_8Cl_{0.9}Br_{0.1}$ as OEP, Ru/$SrTiO_3$:Rh as the HEP, and RGO as electron mediator. When the RGO conductive mediator and CoO_x cocatalyst were decorated on $Bi_4TaO_8Cl_{0.9}Br_{0.1}$ under optimal conditions, an efficient overall water-splitting activity was observed under visible light (Fig. 4e) and UV light (Fig. S13†). H_2 and O_2 were simultaneously evolved at a stoichiometric molar ratio of 2 : 1. The overall water-splitting reaction was carried out in three cycles with steady evolution of H_2 and O_2 over 12 h. The AQY value for this two-step photoexcitation water-splitting system was 1.26% at 420 nm, which is superior to previous reports consisting of metal oxyhalides as OEP. Although the photocatalytic performance for solid-state two-step excitation overall water splitting based on oxyhalide photocatalysts was successfully demonstrated, investigations on the

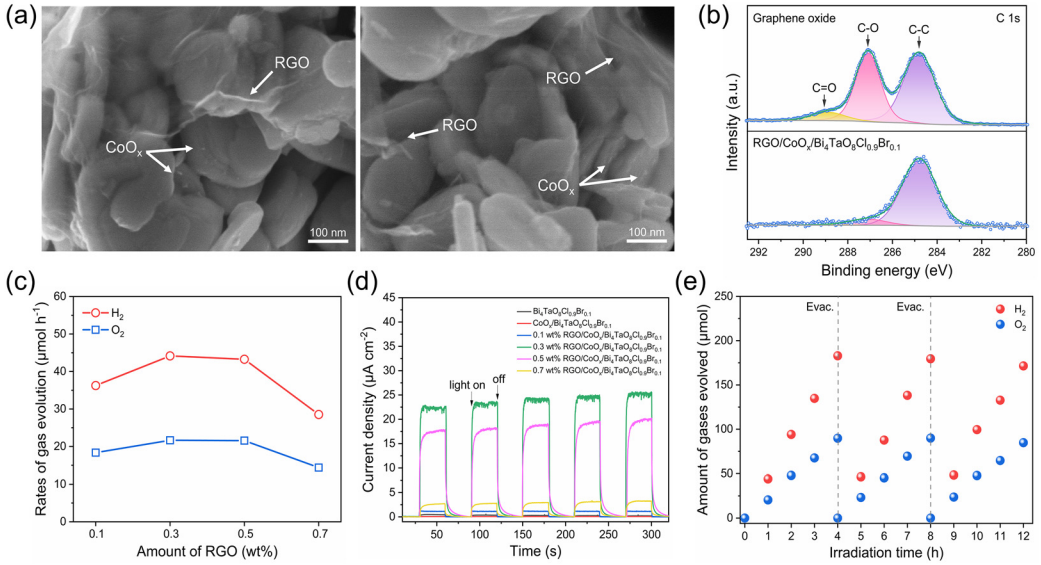

Fig. 4 (a) SEM images of RGO- and CoO_x-co-modified $Bi_4TaO_8Cl_{0.9}Br_{0.1}$. (b) C 1s XPS spectra of graphene oxide (GO) and RGO-modified $Bi_4TaO_8Cl_{0.9}Br_{0.1}$. (c) Photocatalytic activity of the two-step excitation water splitting reaction using RGO- and CoO_x-modified $Bi_4TaO_8Cl_{0.9}Br_{0.1}$ OEP with different RGO contents. Conditions: Ru/$SrTiO_3$:Rh as HEP, 50 mg; surface-modified $Bi_4TaO_8Cl_{0.9}Br_{0.1}$ (CoO_x, 0.5 wt% as Co), 50 mg; 150 mL H_2O, pH = 4; light source, 300 W Xenon lamp ($\lambda \geq 420$ nm). (d) Photocurrent for bare $Bi_4TaO_8Cl_{0.9}Br_{0.1}$ and $Bi_4TaO_8Cl_{0.9}Br_{0.1}$ modified with RGO and/or CoO_x under visible light ($\lambda \geq 420$ nm) at 0.8 V *vs.* RHE. (e) Time course of gas evolution during two-step photoexcitation water splitting reaction under visible light ($\lambda \geq 420$ nm). Conditions: Ru/$SrTiO_3$:Rh as HEP, 50 mg; surface-modified $Bi_4TaO_8Cl_{0.9}Br_{0.1}$ as OEP (CoO_x, 0.5 wt% as Co; RGO, 0.3wt%), 50 mg; 150 mL H_2O, pH = 4; light source, 300 W Xenon lamp ($\lambda \geq 420$ nm).

$Bi_4TaO_8Cl_{0.9}Br_{0.1}$ photocatalyst refinement, RGO decoration methods, and type of solid-state electron mediators are ongoing to further improve the efficiency of overall water splitting.

Conclusions

In summary, an efficient two-step photoexcitation water splitting system using CoO_x-modified $Bi_4TaO_8Cl_{0.9}Br_{0.1}$ as the OEP and RGO as the solid electron mediator was successfully constructed. The formation of a high-crystallinity $Bi_4TaO_8Cl_{0.9}Br_{0.1}$ solid solution synthesized by the dual flux method helped to enhance the light absorption and charge transfer, thus, the O_2-evolution activity of $Bi_4TaO_8Cl_{0.9}Br_{0.1}$ using Fe^{3+} as the electron sacrificial reagent was dramatically improved under visible light irradiation. Upon the modification of $Bi_4TaO_8Cl_{0.9}Br_{0.1}$ with CoO_x cocatalyst and RGO conductive mediator, the charge transfer towards water oxidation reaction and from OEP to HEP was promoted, resulting in the performance enhancement of the two-step excitation water splitting with $Bi_4TaO_8Cl_{0.9}Br_{0.1}$ as OEP and Ru/$SrTiO_3$:Rh as HEP with an AQY of 1.26% at 420 nm, which is higher than that of previous systems consisting of metal oxyhalide photocatalysts. This study verifies the significance and effectiveness of solid solution photocatalyst fabrication and adequate surface modification to boost efficient charge transfer towards practical solar-to-hydrogen energy conversion.

Author contributions

Funding acquisition: Y. Luo, Z. Wang, and H. He. Experimental design and measurements: W. Sun, Y. Luo, J. Xu, Q. Guo, Z. Wang, and H. He. Manuscript writing, revising, and discussion: W. Sun, Y. Luo, L. Deng, Z. Wang, and H. He. All authors gave their approval to the final version of the manuscript.

Conflicts of interest

The authors declare that they have no known competing financial interests or personal relationships that could have appeared to influence the work reported in this paper.

Acknowledgements

This work was financially supported by the General Program (No. 22376207) and the Excellent Young Scientists Fund Program of The National Natural Science Foundation of China, the General Program (No. 2022M723315) of the China Postdoctoral Science Foundation, and CCUS Strategic Priority Program of Research Center for Eco-Environmental Sciences of the Chinese Academy of Sciences of China.

References

1 A. Kudo and Y. Miseki, *Chem. Soc. Rev.*, 2009, **38**, 253–278.
2 N. S. Lewis, *Science*, 2007, **315**, 798.
3 T. Hisatomi and K. Domen, *Nat. Catal.*, 2019, **2**, 387–399.
4 T. Takata, J. Jiang, Y. Sakata, M. Nakabayashi, N. Shibata, V. Nandal, K. Seki, T. Hisatomi and K. Domen, *Nature*, 2020, **581**, 411–414.
5 Y. Qi, Y. Zhao, Y. Y. Gao, D. Li, Z. Li, F. X. Zhang and C. Li, *Joule*, 2018, **2**, 2393–2402.
6 Y. Goto, T. Hisatomi, Q. Wang, T. Higashi, K. Ishikiriyama, T. Maeda, Y. Sakata, S. Okunaka, H. Tokudome, M. Katayama, S. Akiyama, H. Nishiyama, Y. Inoue, T. Takewaki, T. Setoyama, T. Minegishi, T. Takata, T. Yamada and K. Domen, *Joule*, 2018, **2**, 509–520.
7 Z. Wang, Y. Inoue, T. Hisatomi, R. Ishikawa, Q. Wang, T. Takata, S. Chen, N. Shibata, Y. Ikuhara and K. Domen, *Nat. Catal.*, 2018, **1**, 756–763.
8 C. Pan, T. Takata, M. Nakabayashi, T. Matsumoto, N. Shibata, Y. Ikuhara and K. Domen, *Angew. Chem., Int. Ed.*, 2015, **54**, 2955–2959.
9 F. Hou, F. Liu, H. Wu, M. Qasim, Y. Chen, Y. Duan, Z. Feng and M. Liu, *Chin. J. Chem.*, 2023, **41**, 173–180.
10 C. Cheng, L. Mao, X. Kang, C.-L. Dong, Y.-C. Huang, S. Shen, J. Shi and L. Guo, *Appl. Catal., B*, 2023, **331**, 122733.
11 Z. Wang, C. Li and K. Domen, *Chem. Soc. Rev.*, 2019, **48**, 2109–2125.
12 K. Maeda and K. Domen, *J. Phys. Chem. C*, 2007, **111**, 7851–7861.
13 A. Tanaka, K. Teramura, S. Hosokawa, H. Kominami and T. Tanaka, *Chem. Sci.*, 2017, **8**, 2574–2580.
14 Z. Wang, Y. Luo, T. Hisatomi, J. J. M. Vequizo, S. Suzuki, S. S. Chen, M. Nakabayashi, L. H. Lin, Z. H. Pan, N. Kariya, A. Yamakata, N. Shibata, T. Takata, K. Teshima and K. Domen, *Nat. Commun.*, 2021, **12**, 1005.
15 Y. Luo, Q. Q. Guo, J. Xu, H. H. Zhou, Z. Wang and H. He, *Energy Mater. Adv.*, 2022, **2022**, 0003.
16 J. Xu, Y. Luo, Q. Q. Guo, H. H. Zhou, Z. Wang and H. He, *J. Catal.*, 2022, **415**, 19–27.
17 S. Lin, H. Huang, T. Ma and Y. Zhang, *Adv. Sci.*, 2021, **8**, 2002458.
18 K. Ogawa, O. Tomita, K. Takagi, A. Nakada, M. Higashi and R. Abe, *Chem. Lett.*, 2018, **47**, 985–988.
19 Y. Qi, J. W. Zhang, Y. Kong, Y. Zhao, S. S. Chen, D. Li, W. Liu, Y. F. Chen, T. F. Xie, J. Y. Cui, C. Li, K. Domen and F. X. Zhang, *Nat. Commun.*, 2022, **13**, 484.
20 Z. Wang, J. Seo, T. Hisatomi, M. Nakabayashi, J. Xiao, S. Chen, L. Lin, Z. Pan, M. Krause, N. Yin, G. Smith, N. Shibata, T. Takata and K. Domen, *Nano Res.*, 2022, **16**, 4562–4567.
21 X. P. Tao, Y. Zhao, L. C. Mu, S. Y. Wang, R. G. Li and C. Li, *Adv. Energy Mater.*, 2018, **8**, 1701392.
22 A. Nakada, A. Saeki, M. Higashi, H. Kageyama and R. Abe, *J. Mater. Chem. A*, 2018, **6**, 10909–10917.
23 K. Murofushi, K. Ogawa, H. Suzuki, R. Sakamoto, O. Tomita, K. Kato, A. Yamakata, A. Saeki and R. Abe, *J. Mater. Chem. A*, 2021, **9**, 11718–11725.
24 K. Ogawa, H. Suzuki, C. C. Zhong, R. Sakamoto, O. Tomita, A. Saeki, H. Kageyama and R. Abe, *J. Am. Chem. Soc.*, 2021, **143**, 8446–8453.
25 H. Kunioku, M. Higashi, O. Tomita, M. Yabuuchi, D. Kato, H. Fujito, H. Kageyama and R. Abe, *J. Mater. Chem. A*, 2018, **6**, 3100–3107.
26 H. Kunioku, A. Nakada, M. Higashi, O. Tomita, H. Kageyama and R. Abe, *Sustainable Energy Fuels*, 2018, **2**, 1474–1480.
27 H. Suzuki, M. Higashi, H. Kunioku, R. Abe and A. Saeki, *ACS Energy Lett.*, 2019, **4**, 1572–1578.
28 A. Adenle, M. Shi, W. C. Jiang, B. Zeng, C. Li and R. G. Li, *J. Mater. Chem. A*, 2022, **10**, 14293–14299.
29 X. P. Tao, Y. Y. Gao, S. Y. Wang, X. Y. Wang, Y. Liu, Y. Zhao, F. T. Fan, M. Dupuis, R. G. Li and C. Li, *Adv. Energy Mater.*, 2019, **9**, 1803951.
30 X. P. Tao, W. W. Shi, B. Zeng, Y. Zhao, N. Ta, S. Y. Wang, A. A. Adenle, R. G. Li and C. Li, *ACS Catal.*, 2020, **10**, 5941–5948.
31 H. Fujito, H. Kunioku, D. Kato, H. Suzuki, M. Higashi, H. Kageyama and R. Abe, *J. Am. Chem. Soc.*, 2016, **138**, 2082–2085.
32 A. Iwase, Y. H. Ng, Y. Ishiguro, A. Kudo and R. Amal, *J. Am. Chem. Soc.*, 2011, **133**, 11054–11057.
33 K. Maeda, M. Higashi, D. L. Lu, R. Abe and K. Domen, *J. Am. Chem. Soc.*, 2010, **132**, 5858–5868.
34 M. X. Hu, S. W. Du, B. B. Dong, Y. Qi, Z. C. Feng and F. X. Zhang, *J. Mater. Chem. A*, 2022, **10**, 16541–16546.
35 Y. Sasaki, H. Nemoto, K. Saito and A. Kudo, *J. Phys. Chem. C*, 2009, **113**, 17536–17542.
36 Q. Wang, T. Hisatomi, Q. X. Jia, H. Tokudome, M. Zhong, C. Z. Wang, Z. H. Pan, T. Takata, M. Nakabayashi, N. Shibata, Y. B. Li, I. D. Sharp, A. Kudo, T. Yamada and K. Domen, *Nat. Mater.*, 2016, **15**, 611–615.
37 Q. Wang, T. Hisatomi, Y. Suzuk, Z. H. Pan, J. Seo, M. Katayama, T. Minegishi, H. Nishiyama, T. Takata, K. Seki, A. Kudo, T. Yamada and K. Domen, *J. Am. Chem. Soc.*, 2017, **139**, 1675–1683.
38 Q. Wang, S. Okunaka, H. Tokudome, T. Hisatomi, M. Nakabayashi, N. Shibata, T. Yamada and K. Domen, *Joule*, 2018, **2**, 2667–2680.
39 S. S. K. Ma, K. Maeda, T. Hisatomi, M. Tabata, A. Kudo and K. Domen, *Chem. – Eur. J.*, 2013, **19**, 7480–7486.
40 K. Iwashina, A. Iwase, Y. H. Ng, R. Amal and A. Kudo, *J. Am. Chem. Soc.*, 2015, **137**, 604–607.
41 Z. Pan, G. Zhang and X. Wang, *Angew. Chem., Int. Ed.*, 2019, **58**, 7102–7106.
42 R. Konta, T. Ishii, H. Kato and A. Kudo, *J. Phys. Chem. B*, 2004, **108**, 8992–8995.
43 K. Ogawa, A. Nakada, H. Suzuki, O. Tomita, M. Higashi, A. Saeki, H. Kageyama and R. Abe, *ACS Appl. Mater. Interfaces*, 2019, **11**, 5642–5650.

44 X. P. Tao, Y. Zhao, S. Y. Wang, C. Li and R. G. Li, *Chem. Soc. Rev.*, 2022, **51**, 3561–3608.
45 Z. H. Pan, T. Hisatomi, Q. Wang, S. S. Chen, A. Iwase, M. Nakabayashi, N. Shibata, T. Takata, M. Katayama, T. Minegishi, A. Kudo and K. Domen, *Adv. Funct. Mater.*, 2016, **26**, 7011–7019.
46 Y. H. Ng, A. Iwase, A. Kudo and R. Amal, *J. Phys. Chem. Lett.*, 2010, **1**, 2607–2612.